Nanoscale

ROYAL SOCIETY OF CHEMISTRY

PAPER

View Article Online
View Journal

Check for updates

Cite this: DOI: 10.1039/d5nr04517g

Rational design of self-assembled monolayer composition for efficient perovskite/Si tandem solar cells

Min Sup Kim, †[a] So Jeong Park, †[a] Geon Pyo Hong [a] and Jin Young Kim *[a,b,c]

Efficient charge extraction at the interface is essential for achieving high-performance perovskite/Si tandem solar cells. Here, we demonstrate a highly efficient wide-bandgap perovskite single-junction solar cell using a co-adsorption strategy of commercial self-assembled monolayers (SAMs), specifically MeO-4PACz and Br-4PACz. Mixed-SAMs, with electron-withdrawing Br functional groups, induce a larger dipole moment and a downward shift in the HOMO level, thereby promoting favorable energy level alignment with a wide-bandgap perovskite. It further passivates interfacial defects, suppressing non-radiative recombination. This combined effect enables effective hole transport at the SAM/perovskite interface, enhancing the open-circuit voltage and fill factor of the perovskite device. Accordingly, the optimal single-junction perovskite solar cell exhibits an efficiency of 19.72%. By integrating this cell with a Si bottom cell, we achieve a tandem solar cell efficiency of 28.02%. This study provides a universal strategy to design SAM-based interfacial layers in p-i-n perovskite and tandem solar cells.

Received 27th October 2025,
Accepted 1st March 2026

DOI: 10.1039/d5nr04517g

rsc.li/nanoscale

Introduction

Perovskite/Si tandem solar cells have emerged as a leading candidate for next-generation photovoltaics, capable of surpassing the Shockley–Queisser limit of single-junction solar cells.[1–4] Significant advances have been achieved in recent years, with the certified efficiency of perovskite/Si tandem solar cells reaching 34.9%.[5] Within these tandem structures, carbazole-based self-assembled monolayers (SAMs) have been widely employed as hole-selective materials due to their superior hole-transporting properties, minimal parasitic absorption, and tunable energy levels.[6–9] To fully utilize these advantages, further optimization is required for wide-bandgap perovskites in tandem solar cells. Previous studies have employed molecular and compositional engineering of SAMs to passivate interfacial defects and achieve favorable energy level alignment, thereby enabling efficient charge transport at the SAM/perovskite interface.[10–12]

Since Albrecht *et al.* introduced [2-(9*H*-carbazol-9-yl)ethyl] phosphonic acid (2PACz) featuring a carbazole core and a phosphonic acid anchoring group,[13] methoxy- and methyl-functionalized derivatives have been developed to enhance hole extraction at the SAM/perovskite interface.[14] In addition, tailoring the anchoring and functional groups of SAM molecules altered their dipole moment, energy level, and wettability, thereby mitigating interfacial defects and improving energy level alignment.[15–17] Although such modifications of molecular structures are effective in further enhancing the device performance, they often require complex synthesis processes, imposing considerable challenges for practical applications. To overcome the inherent limitations of single-component approaches, a co-adsorption strategy incorporating additional molecular species has been employed. Zhao *et al.* blended a non-planar molecule, 3,3-(4-amino-4*H*-1,2,4-triazole-3,5-diyl)-dibenzo acid (ABT) with [4-(3,6-dimethyl-9*H*-carbazol-9-yl) butyl]phosphonic acid (Me-4PACz), forming a densely packed layer that improves interfacial bonding and reduces tensile strain.[18] Harter *et al.* achieved over 30% stabilized efficiency in perovskite/Si tandem solar cells by co-adsorbing functionalized phosphonic acids to improve the wettability of the Me-4PACz layer.[19] However, these additive incorporation strategies can also induce trade-offs, including slower hole extraction and unfavorable shifts in the work function of tandem solar cells.[20] Therefore, a facile and versatile approach is needed to realize superior interfacial properties while maintaining compatibility with tandem solar cells.

In this study, we develop a feasible and efficient co-adsorption strategy that utilizes a mixture of commercial SAM mole-

---

[a] *Department of Materials Science and Engineering, Seoul National University, Seoul 08826, Republic of Korea. E-mail: jykim.mse@snu.ac.kr*

[b] *Research Institute of Advanced Materials (RIAM), Seoul National University, Seoul 08826, Republic of Korea*

[c] *School of Transdisciplinary Innovations, Seoul National University, Seoul 08826, Republic of Korea*

† These authors contributed equally to this work.

cules (4-(3,6-dimethoxy-9*H*-carbazol-9-yl)butyl)phosphonic acid (MeO-4PACz) and (4-(3,6-dibromo-9*H*-carbazol-9-yl)butyl) phosphonic acid (Br-4PACz). By introducing a SAM functionalized with electron-withdrawing Br groups, the work function (WF) was increased and the highest occupied molecular orbital (HOMO) level was lowered, enabling favorable energy level alignment with the wide-bandgap perovskite absorber layer. Furthermore, the introduction of the Br groups suppressed trap-assisted recombination. As a result, hole extraction at the SAM/perovskite interface was enhanced, leading to improvements in both V_{OC} and FF in perovskite single-junction devices and recording a conversion efficiency of 19.72%. By integrating the perovskite cell on top of a Si bottom cell, a monolithic perovskite/Si tandem solar cell with an efficiency of 28.02% could be achieved.

Results and discussion

Tailoring SAM composition

Fig. 1A presents the molecular structures and co-adsorption strategy of SAM molecules with different substituents, including MeO– and Br– groups. The preferential orientation of SAM terminal groups toward the perovskites affects the interfacial characteristics. While the MeO-substituent is known to passivate defects at SAM/perovskite interfaces, symmetrically positioned terminal groups can reduce dipole moment.[13,14] This reduced dipole moment decreases the WF, impeding hole extraction between the perovskite and SAM.[21] On the other hand, the electron-withdrawing Br-substituent alters electron cloud density on the carbazole core, resulting in an increased dipole moment and a downward shift in the HOMO level.[22–25]

To investigate the effect of the Br-substituent on energy level alignment, we varied the mixing ratio of MeO- and Br-substituents. The detailed conditions of the mixing ratio are provided in the Experimental section (SI). A representative mixed-SAM with a Br : MeO mixing ratio of 4 : 1 was selected because a noticeable work function (WF) shift emerged at this ratio, and results for other ratios are shown in Fig. S1. Fig. 1B shows the ultraviolet photoelectron spectroscopy (UPS) spectra in the valence band onset and secondary cut-off regions, comparing the WF and valence band maximum level (E_{VB}) of MeO-4PACz, mixed-SAM, and Br-4PACz. The WFs of MeO-4PACz, mixed-SAM, and Br-4PACz are 4.72, 4.92, and 4.97 eV, respectively, revealing that the WF of SAM molecules increases with the increasing Br ratio. More negative contact potential difference (CPD) values with higher Br ratios, as measured by Kelvin probe force microscopy (KPFM), further confirm the increase in WF (Fig. 1C).

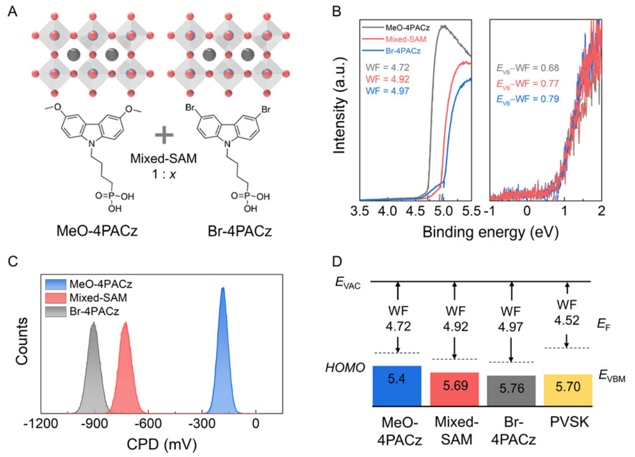

Fig. 1 Electrical properties of the SAMs. (A) Schematic diagram of the co-adsorption strategy and the molecular structures of MeO-4PACz and Br-4PACz. (B) UPS spectra representing the secondary electron cut-off and valence band off-set regions. (C) Contact potential difference histogram of the various SAMs obtained from KPFM. (D) Energy band diagram of the various SAMs and perovskite absorber layers.[26]

Fig. 1D shows the energy band diagram of various SAM molecules and perovskites measured by UPS. The electron-withdrawing nature of the Br-substituent reduces the electron cloud density,[25,27] resulting in the lower HOMO levels of Br-4PACz (−5.76 eV) and mixed-SAM (−5.69 eV) compared to MeO-4PACz (−5.4 eV). This trend is clearly observed for various mixing ratios (Fig. S2), indicating that favorable alignment with perovskites can be achieved by adjusting the SAM composition.

Perovskite cell performance

To examine the influence of the Br-substituent on device performance, we fabricated single-junction wide-bandgap perovskite solar cells consisting of an ITO/SAM/perovskite/C_{60}/PEIE/Ag structure. The composition of the wide-bandgap (E_g = 1.67 eV) perovskite is $Cs_{0.05}(FA_{0.77}MA_{0.23})_{0.95}Pb(I_{0.77}Br_{0.23})_3$ (Fig. S3), which is suitable for application in perovskite/Si tandem solar cells. Fig. 2A shows the current density–voltage (*J*–*V*) curves of perovskite devices for various Br : MeO ratios. The photovoltaic and diode parameters derived from the dark *J*–*V* curves are summarized in Table S1. According to our preliminary experiments (Fig. S4), the optimal Br : MeO ratio was demonstrated to be 4 : 1, as noted for the mixed-SAM. The device incorporating a pure Br-4PACz SAM did not function properly, likely due to poor junction properties characterized by high series resistance (R_S = 635.79 Ω cm^2) and a low FF. One possible origin of the high R_S is inappropriate energy band alignment with the perovskite layer.[28–30] A direct comparison between MeO-4PACz and mixed-SAM reveals that Br substitution enhances power conversion efficiency (PCE), notably increasing the open-circuit voltage (V_{OC}) and FF, owing to improved energy level alignment at the SAM/perovskite interface. However, there are no significant changes in the short-circuit current density (J_{SC}). This tendency is further demonstrated in the statistical photovoltaic parameters shown in Fig. 2B. Consequently, the best-performing mixed-SAM-based device achieved the best PCE of 19.72% with a J_{SC} of 20.41 mA cm^{-2}, a V_{OC} of 1.20 V, and a FF of 0.81. Fig. 2C shows the external quantum efficiency (EQE) curves and integrated J_{SC} of the perovskite device, with no considerable difference between the MeO-4PACz and mixed-SAM, which is con-

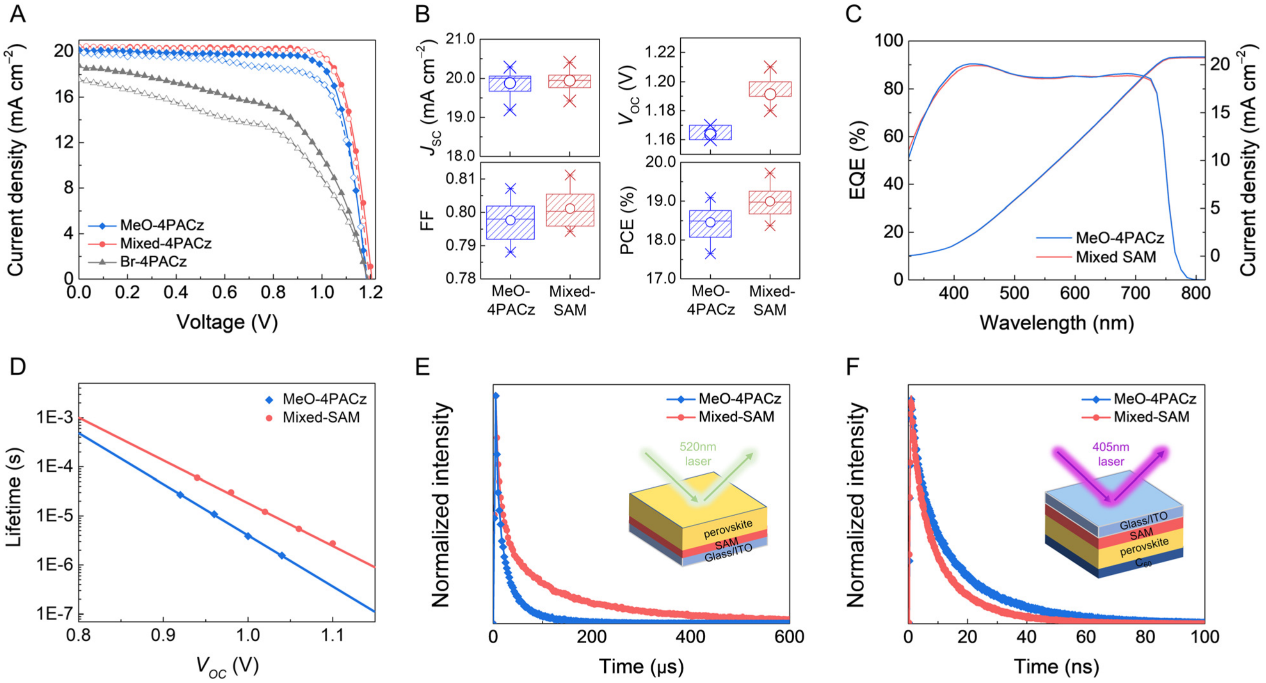

Fig. 2 Single-junction device characteristics and charge dynamics (A) *J*–*V* curves of the champion perovskite single-junction solar cells. (B) Statistical photovoltaic parameters of the perovskite device with MeO-4PACz and a mixed-SAM. This statistical representation shows the minimum and maximum values as crosses, the mean value as a circle, and the box indicating the 25th to 75th percentile range. (C) EQE and integrated J_{SC} curves. (D) Lifetime calculated from EIS results using the equation $\tau = 1/(2\pi f_{max})$, where f_{max} is the characteristic frequency in the Bode plot. (E and F) TR-PL decay curves of the perovskite layers. The schematic of (E) shows the results from perovskite-side excitation of the ITO/SAM/perovskite film using a 520 nm laser, while the schematic of (F) shows the spectra from SAM-side excitation of the ITO/SAM/perovskite/C_{60} film with a 405 nm laser.

sistent with the J_{SC} obtained by *J*–*V* curves. The Br functional groups were found to have a negligible effect on the absorbance, grain morphology, and crystallinity of the perovskite absorber layers (Fig. S5–7), yielding comparable J_{SC} for both SAMs.[28]

The electrochemical impedance spectroscopy (EIS) reveals that the charge carrier lifetime of the mixed-SAM (5.458 μs) is longer than that of MeO-4PACz (0.928 μs), as shown in Fig. 2D,[29,30] which is consistent with the transient photovoltage decay (TPVD) curves (Fig. S8) showing an extended charge carrier lifetime of the mixed-SAM. These observations can be ascribed to the effective defect passivation at the SAM/perovskite interface by the Br substituent.[31] The semicircle in the low frequency region of the Nyquist plot (Fig. S9), corresponding to the charge recombination resistance (R_{rec}), reveals that the mixed-SAM has a higher R_{rec} (126.41 Ω for the mixed-SAM and 21.5 Ω for MeO-4PACz), further supporting suppressed charge recombination by Br substitution.[32,33] These results suggest that both interfacial energy alignment and defect suppression contribute to the enhancement of V_{OC}. To investigate the charge transfer characteristics at the SAM/perovskite interfaces, we conducted steady-state (SS) and time-resolved (TR) photoluminescence (PL) measurements. Fig. 2E and F present TR-PL curves, while the inset illustrates the sample structure, the excitation wavelength, and the laser irradiation direction. The penetration depth varies with the excitation wavelength (Fig. S10). For instance, the 405 nm laser probes the surface (~27 nm), whereas the 520 nm laser extends into bulk (~217 nm).[10,17,34,35] Under 520 nm excitation from the perovskite side, the mixed-SAM exhibits a longer average carrier lifetime (τ_{avg} = 34.8 μs) than MeO-4PACz (τ_{avg} = 22.3 μs). This is consistent with higher SS-PL intensity observed in the mixed-SAM, indicating reduced non-radiative recombination (Fig. S11).[36,37] Meanwhile, the mixed-SAM shows a faster decay under 405 nm excitation from the SAM side, resulting from improved interfacial charge extraction.[38,39] Under these excitation conditions, both MeO-4PACz and mixed-SAM samples exhibit a comparable degree of quenching (Fig. S12).[34] Therefore, the enhanced FF by the Br substitution can be attributed to the facilitated hole extraction at the SAM/perovskite interface.

Tandem cell performance

We fabricated two-terminal (2T) perovskite/Si tandem solar cells using the best wide-bandgap perovskite solar cell incorporating the mixed-SAM layer. Further details about the tandem device fabrication are provided in the Experimental section. Prior to the tandem integration, the single-junction transparent perovskite solar cell was optimized to enable light illumination from the top electrode rather than the glass substrate. The resulting semi-transparent perovskite solar cell exhibits a J_{SC} of 19.37 mA cm^{-2}, a V_{OC} of 1.20 V, a FF of 76.7%,

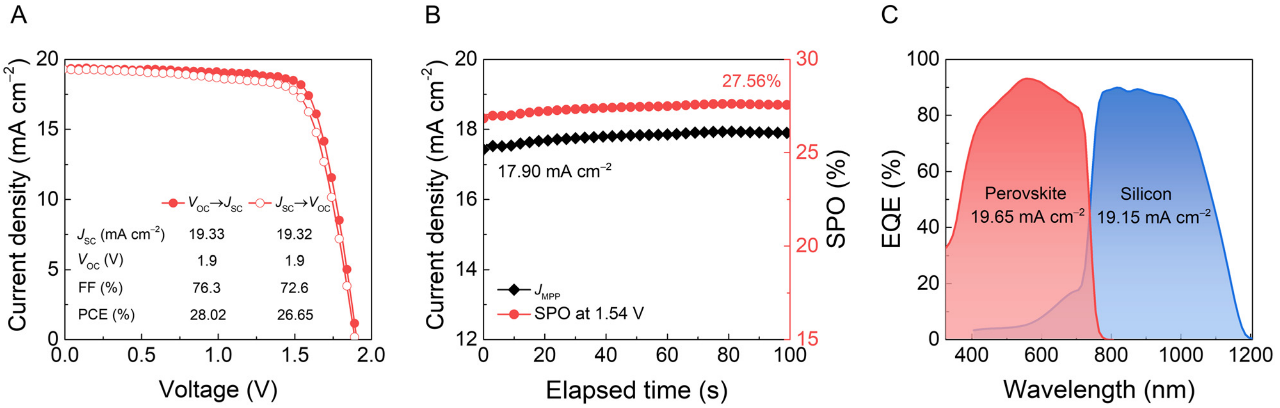

Fig. 3 Tandem device performance. (A) *J*–*V* curves, (B) SPO measured at the maximum power point, and (C) EQE spectra of each subcell of the champion 2T perovskite/Si tandem solar cells.

and a PCE of 17.81%, with an aperture size of 0.1875 cm^2 (Fig. S13). Fig. 3A shows the *J*–*V* curve of the best performing perovskite/Si tandem solar cell consisting of a silicon heterojunction (SHJ) bottom cell and a mixed-SAM-based perovskite top cell. This device exhibits a J_{SC} of 19.33 mA cm^{-2}, a V_{OC} of 1.90 V, a FF of 76.3%, and a PCE of 28.02%, with an aperture size of 1 cm^2. The steady-state power output (SPO) curve yields a stabilized PCE of 27.56% (Fig. 3B). Fig. 3C presents the J_{SC} of each sub-cell, demonstrating effective current matching between the top and bottom cells, with values comparable to those derived from the *J*–*V* curve.

Conclusion

We examined the effects of the functional groups in SAM molecules by varying the mixing ratios between MeO-4PACz and Br-4PACz. Incorporation of the electron-withdrawing Br-substituent induced a downward shift in the HOMO level of SAM molecules, leading to a favorable energy band alignment with the wide-bandgap perovskite absorber. It also enabled efficient hole extraction at the SAM/perovskite interface. Furthermore, the Br-substituent alleviated interfacial defects, effectively reducing charge recombination losses. The combined effects of accelerated charge extraction and suppressed non-radiative recombination at the SAM/perovskite interface significantly enhanced the V_{OC} and FF of the single-junction perovskite solar cell. By integrating the optimized perovskite top cell with a SHJ bottom cell, we achieved a 2T perovskite/Si tandem solar cell with a PCE of 28.02%. The effect of mixing SAM molecules investigated in this study offers a simple yet effective strategy to tune the electronic properties of SAMs for highly efficient p-i-n perovskite solar cells and tandem devices.

Author contributions

M. S. K. carried out the overall experiments, including device fabrication and characterization. P. S. J. contributed to the conceptual development of the study, provided critical feedback throughout the research, and fabricated the tandem solar cells. G. P. H. assisted with the stability analysis of the tandem devices. J. Y. K. contributed to conceptual discussions and managed and supervised the research project.

Conflicts of interest

The authors declare no competing interests.

Data availability

The data supporting this article have been included as part of the supplementary information (SI). Supplementary information is available. See DOI: https://doi.org/10.1039/d5nr04517g.

Acknowledgements

This work was supported by the National Research Foundation of Korea (NRF) grant funded by the Korean government (MSIT) (RS-2023-00273532) and the Korea Institute of Energy Technology Evaluation and Planning (KETEP), and the Ministry of Trade, Industry and Energy (MOTIE) of the Republic of Korea (RS-2023-00302107). This work was supoted by Mid-Career Bridging Program through Seoul National University.

References

1 H. Zhou, *et al.*, Interface engineering of highly efficient perovskite solar cells, *Science*, 2014, **345**(6196), 542–546.
2 Y. Li, *et al.*, Recent progress of critical interface engineering for highly efficient and stable perovskite solar cells, *Adv. Energy Mater.*, 2022, **12**(5), 2102730.

3 A. U. I. Shah and E. L. Meyer, Perovskite-based solar cells in photovoltaics for commercial scalability: Current progress, challenges, mitigations and future prospectus, *Sol. Energy*, 2025, **286**, 113172.

4 C. Yang, *et al.*, Achievements, challenges, and future prospects for industrialization of perovskite solar cells, *Light: Sci. Appl.*, 2024, **13**(1), 227.

5 M. A. Green, *et al.*, *Solar Cell Efficiency Tables (Version 65)*, 2024.

6 Y. Duan, *et al.*, A Comprehensive Review of Organic Hole–Transporting Materials for Highly Efficient and Stable Inverted Perovskite Solar Cells, *Adv. Funct. Mater.*, 2024, **34**(25), 2315604.

7 M. Azam, *et al.*, Dual functionality of charge extraction and interface passivation by self-assembled monolayers in perovskite solar cells, *Energy Environ. Sci.*, 2024, **17**(19), 6974–7016.

8 W. Li, E. Martínez-Ferrero and E. Palomares, Self-assembled molecules as selective contacts for efficient and stable perovskite solar cells, *Mater. Chem. Front.*, 2024, **8**(3), 681–699.

9 M. Li, *et al.*, Self-assembled monolayers for interfacial engineering in solution-processed thin-film electronic devices: design, fabrication, and applications, *Chem. Rev.*, 2024, **124**(5), 2138–2204.

10 Z. Iqbal, *et al.*, Interface modification for energy level alignment and charge extraction in CsPbI3 perovskite solar cells, *ACS Energy Lett.*, 2023, **8**(10), 4304–4314.

11 D. Song, *et al.*, Toward Maximizing Hole Selection with Self-Assembled Monolayers in Sn-Based Perovskite Solar Cells, *ACS Energy Lett.*, 2025, **10**(3), 1292–1312.

12 G. Qu, *et al.*, Conjugated linker-boosted self-assembled monolayer molecule for inverted perovskite solar cells, *Joule*, 2024, **8**(7), 2123–2134.

13 A. Al-Ashouri, *et al.*, Conformal monolayer contacts with lossless interfaces for perovskite single junction and monolithic tandem solar cells, *Energy Environ. Sci.*, 2019, **12**(11), 3356–3369.

14 A. Al-Ashouri, *et al.*, Monolithic perovskite/silicon tandem solar cell with >29% efficiency by enhanced hole extraction, *Science*, 2020, **370**(6522), 1300–1309.

15 C. Guo, *et al.*, Bifacially Reinforced Self–Assembled Monolayer Interfaces for Minimized Recombination Loss and Enhanced Stability in Perovskite/Silicon Tandem Solar Cells, *Adv. Mater.*, 2025, 2504520.

16 C. Li, *et al.*, Achieving 32% Efficiency in Perovskite/Silicon Tandem Solar Cells with Bidentate–Anchored Superwetting Self–Assembled Molecular Layers, *Angew. Chem.*, 2025, e202502730.

17 S. J. Park, *et al.*, Tailored self-assembled monolayer molecules for perovskite/PERC tandem solar cells with efficiencies over 30%, *Energy Environ. Sci.*, 2025, **18**(20), 9105–9113.

18 H. Zhao, *et al.*, Synergistic Self–Assembled Monolayers Reinforce Buried Interface Anchoring for High–Efficiency Tandem Perovskite Solar Cells, *Angew. Chem.*, 2025, **137**(36), e202504237.

19 A. Harter, *et al.*, Perovskite/silicon tandem solar cells above 30% conversion efficiency on submicron-sized textured Czochralski-silicon bottom cells with improved hole-transport layers, *ACS Appl. Mater. Interfaces*, 2024, **16**(45), 62817–62826.

20 K. Hossain, *et al.*, Resolving the hydrophobicity of the Me-4PACz hole transport layer for inverted perovskite solar cells with efficiency> 20%, *ACS Energy Lett.*, 2023, **8**(9), 3860–3867.

21 W. Peng, *et al.*, A versatile energy-level-tunable hole-transport layer for multi-composition inverted perovskite solar cells, *Energy Environ. Sci.*, 2025, **18**(2), 874–883.

22 L. V. T. Merino, *et al.*, Impact of the valence band energy alignment at the hole-collecting interface on the photostability of wide band-gap perovskite solar cells, *Joule*, 2024, **8**(9), 2585–2606.

23 Q. Chen, *et al.*, Interfacial dipole in organic and perovskite solar cells, *J. Am. Chem. Soc.*, 2020, **142**(43), 18281–18292.

24 B. De Boer, *et al.*, Tuning of metal work functions with self–assembled monolayers, *Adv. Mater.*, 2005, **17**(5), 621–625.

25 E. Arkan, *et al.*, Effect of functional groups of self assembled monolayer molecules on the performance of inverted perovskite solar cell, *Mater. Chem. Phys.*, 2020, **254**, 123435.

26 G. Wang, *et al.*, Molecular engineering of hole-selective layer for high band gap perovskites for highly efficient and stable perovskite-silicon tandem solar cells, *Joule*, 2023, **7**(11), 2583–2594.

27 Y. Lin, *et al.*, 18.4% organic solar cells using a high ionization energy self–assembled monolayer as hole–extraction interlayer, *ChemSusChem*, 2021, **14**(17), 3569–3578.

28 I. Levine, *et al.*, Charge transfer rates and electron trapping at buried interfaces of perovskite solar cells, *Joule*, 2021, **5**(11), 2915–2933.

29 E. Von Hauff and D. Klotz, Impedance spectroscopy for perovskite solar cells: characterisation, analysis, and diagnosis, *J. Mater. Chem. C*, 2022, **10**(2), 742–761.

30 I. J. Park, *et al.*, A three-terminal monolithic perovskite/Si tandem solar cell characterization platform, *Joule*, 2019, **3**(3), 807–818.

31 W. Tress, *et al.*, Understanding the rate-dependent J–V hysteresis, slow time component, and aging in CH 3 NH 3 PbI 3 perovskite solar cells: the role of a compensated electric field, *Energy Environ. Sci.*, 2015, **8**(3), 995–1004.

32 Q. Zhuang, *et al.*, Tailoring multifunctional anion modifiers to modulate interfacial chemical interactions for efficient and stable perovskite solar cells., *Nano Energy*, 2022, **102**, 107747.

33 A. Yi, *et al.*, Room-temperature-processed perovskite solar cells surpassing 24% efficiency, *Joule*, 2024, **8**(7), 2087–2104.

34 J. Maes, *et al.*, Light absorption coefficient of $CsPbBr_3$ perovskite nanocrystals, *J. Phys. Chem. Lett.*, 2018, **9**(11), 3093–3097.
35 G. Zhou, *et al.*, Perovskite Solar Cells Modified with Conjugated Self-Assembled Monolayers at Buried Interfaces, *Nanomaterials*, 2025, **15**(13), 1014.
36 D. W. de Quilettes, *et al.*, Impact of microstructure on local carrier lifetime in perovskite solar cells, *Science*, 2015, **348**(6235), 683–686.
37 S. Xiong, *et al.*, Reducing nonradiative recombination for highly efficient inverted perovskite solar cells via a synergistic bimolecular interface, *Nat. Commun.*, 2024, **15**(1), 5607.
38 E. Kasparavičius, *et al.*, Charge carrier dynamics at the perovskite interface with self-assembled monolayers, *ACS Appl. Mater. Interfaces*, 2024, **16**(43), 59477–59487.
39 X. Chen, *et al.*, Charge transfer kinetics in halide perovskites: On the constraints of time-resolved spectroscopy measurements, *ACS Energy Lett.*, 2024, **9**(6), 3187–3203.